# Optical photothermal infrared imaging using metabolic probes in biological systems

Sydney O. Shuster, Anna E. Curtis, and Caitlin M. Davis*

Department of Chemistry, Yale University, New Haven, Connecticut 06511, United States

**ABSTRACT:** Infrared spectroscopy is a powerful tool for identifying biomolecules. In biological systems, infrared spectra provide information on structure, reaction mechanisms, and conformational change of biomolecules. However, the promise of applying infrared imaging to biological systems has been hampered by low spatial resolution and the overwhelming water background arising from the aqueous nature of in cell and *in vivo* work. Recently, optical photothermal infrared microscopy (OPTIR) has overcome these barriers and achieved both spatially and spectrally resolved images of live cells and organisms. Here, we determine the most effective modes of collection for work in biological samples. We examine three cell lines (Huh-7, differentiated 3T3-L1, and U2OS) and three organisms (*E. coli*, tardigrades, and zebrafish). Our results suggest that the information provided by multifrequency imaging is comparable to hyperspectral imaging while reducing imaging times twenty-fold. We also explore the utility of IR active probes, including global and site-specific probes, for tracking metabolic pathways and protein localization, structure, and local environment. Our findings illustrate the versatility of OPTIR, and together, provide a direction for future dynamic imaging of living cells and organisms.

## INTRODUCTION

Vibrational microspectroscopy has shown significant promise as a technique for understanding biophysical and biological processes. Infrared and Raman based techniques can provide detailed insight for complex sample identification without the need for bulky, disruptive labels.[1–4] Vibrational techniques can also be used to assign protein secondary structure,[5] observe changes in folding,[6] and follow metabolic processes using isotope labels.[3] Yet, use of vibrational imaging has been limited in cell biology and biophysics. Raman imaging suffers from weak cross-sections necessitating high laser powers. Stimulated Raman scattering has been invaluable due to its increased signal intensity, but collecting full spectrum is nontrivial, limiting its use.[4,7] Infrared imaging, on the other hand, has not been used significantly outside ‘stainless histology’ and dry, fixed cell work because of the strong background absorption from water and poor diffraction limits.[8,9]

Optical photothermal infrared microscopy (OPTIR), also known as mid-infrared photothermal imaging (MIP), is a new and promising technique in the biological and chemical sciences.[10–13] OPTIR is a pump-probe technique in which a sample is pumped with a pulsed, tunable infrared laser.[10,11] Upon absorption of the infrared light, the sample heats according to the photothermal effect. This heating causes thermal expansion and a change in the refractive index of the sample which can be probed by a visible laser. By detecting the visible laser, changes in its intensity that match the pulse rate of the infrared laser can be extracted and used to generate an infrared spectrum that corresponds well with the FTIR spectrum. This technique is analogous to AFM-IR with an optical probe instead of a physical probe.

OPTIR brings significant benefits to biophysics and biology. As a vibrational method, OPTIR allows for detailed spectral information on samples including label free identification of biopolymers and assignments of protein structures.[14] Low laser powers are non-perturbative to the system.[15] According to Onsanger’s fluctuation dissipation theorem[16], the kinetics following a small perturbation away from equilibrium are identical to the natural kinetics observed by spontaneous fluctuations. Therefore, small <3 K perturbations introduced by OPTIR lasers mimic native fluctuations.[15] Furthermore, OPTIR has a spatial resolution of under 500 nm and is less impacted by water absorption as water’s high heat capacity reduces its photothermal signal. Because of this, OPTIR can be used to collect vibrational images in living cells and tissues in water. Past work has demonstrated that OPTIR can be used to collect both single frequency images and full spectra in live cells.[12,17,18] Additionally, hyperspectral images have been collected in fixed and dried tissues.[13,17] These techniques have been used to track lipid[15,17,18] and carbohydrate[19] metabolism in cells and identify protein aggregation in tissues.[20]

Vibrational probes used with OPTIR include isotope labels, such as $^{13}C$ and $^{2}H$, and small IR active moieties, such as azides and nitriles. Carbon deuterium, azide, and nitrile moieties absorb at ~2100 $cm^{-1}$ which falls into the “cellular silent region” where other cellular biomolecules do not absorb allowing for easy discernment of the labeled substrate from cellular background. This region has been used with significant success in spontaneous Raman[21] and SRS[22] with alkyne moieties.

OPTIR has the potential to be most informative in living cells, tissues, and organisms where cellular processes could be measured in a tag-free manner or using small IR probes. Although OPTIR shows significant promise, it has been limited by slower acquisition times (in the case of hyperspectral images) and limited spectral information (in the case of single frequency images). Here we examine corrected single frequency imaging and multispectral ratio imaging as compared to hyperspectral imaging of fixed cells to assess the accuracy of multispectral imaging. We conclude that when properly corrected for and used for ratio imaging, multispectral images can provide similar information to hyperspectral images with 1/20th of the collection time. We further highlight the compatibility of the technique with various cell lines and model organisms including live cell culture in water. Further, we use several infrared probes across protein and lipid metabolism including 4-azidomethyl-L-phenylalanine (AzmF) incorporated at a single site in sfGFP to demonstrate a site-specific protein infrared probe detected using OPTIR. This lays the groundwork for future OPTIR studies of metabolic processes in live cells and organisms.

## METHODS

**Materials.** Unless otherwise specified, all reagents were sourced from Sigma-Aldrich.

**Oleic Acid Conjugation and Feeding Protocol.** Oleic acid conjugation and feeding was performed as previously described.[18] Briefly, $^2$H oleic acid (oleic acid-$d_{33}$, DLM-1891-PK, Cambridge Isotope Laboratories, Tewksbury, MA) was bound to fatty acid-free bovine serum albumin (BSA) using a protocol from Shi et al.[3] The stock oleic acid concentration is approximately 3 mM. The ratio of oleic acid to BSA is 2:1, in line with physiological ratios.[23,24] Oleic acid is then incubated with cell culture at a concentration of 60 μM.

**Mammalian cell culture.** Huh-7 cells (gift from Lars Plate, Vanderbilt University) and U2OS cells (ATCC, Manassas, VA) were prepared as previously described.[17,18] Briefly, cells were cultured in 75 $cm^3$ sterile vented cap tissue culture flasks (Corning, Corning, NY). At 80 % confluence, cells were trypsinized and replated on $CaF_2$ coverslips (20 x 20 x 0.35 mm, Crystran, Poole, U.K.) in 35 mm diameter sterile Petri dishes (Corning) for live samples and $CaF_2$ coverslips (10 x 0.35 mm) in a 24 well cell culture plate (Corning) for fixed samples. Cells were allowed to adhere for 24 hours prior to experimentation.

3T3-L1 cells (ATCC, Manassas, VA) were prepared as previously described.[17] Briefly, low passage number (<10), predifferentiated cells were grown to confluence in Dulbecco's modified Eagle's medium containing 4.5 g/L glucose and L-glutamine (DMEM, Corning) supplemented with 10% calf bovine serum (CBS, ATCC) and 1% penicillin/streptomycin (Thermo-Fischer) under standard conditions. Two to three days post confluence the cells were differentiated, media was changed to DMEM containing 10% fetal bovine serum (FBS, Corning), 1% penicillin/streptomycin, 20 μg/mL insulin, 250 nM dexamethasone, and 500 μM isobutylmethylxanthine. Two to three days post differentiation, media was changed to DMEM containing 10% fetal bovine serum (FBS, Corning), 1% penicillin/streptomycin and 20 μg/mL insulin. Following another two to three days, cells were trypsinized and replated on $CaF_2$ coverslips (20 x 20 x 0.35 mm; Crystran.) in 35 mm dishes (Corning). Media was exchanged every two to three days until lipid droplets formed and stabilized (five to seven days).

**$^{13}$C and $^2$H labeling mammalian cells.** Medium was replaced with glucose-free DMEM supplemented with 1% FBS, 1% penicillin/streptomycin, $^{13}$C glucose (D-glucose-$^{13}C_6$, CLM-1396-PK, Cambridge Isotope Laboratories) to 4.5 mg/mL, and either 2% BSA or 2% $^2$H oleic acid conjugated with BSA (final concentration 60 μM oleic acid and 30 μM BSA).

**$^{13}$C labeling *E. coli*.** BL21(DE3) strain *E. coli* were transformed with empty pUC-19 vectors to encode ampicillin resistance. Several colonies were selected and grown in 5 mL of Luria broth (LB) at 37 °C with 300 rpm shaking overnight. 200 μL of starter was transferred to 5 mL of M9 media supplemented with $^{13}$C labeled glucose or LB (control) and grown until cloudy, then 1 mL was moved to 20 mL of M9 supplemented with $^{13}$C labeled glucose and grown until an OD at 600 nm of 0.6-0.8. The temperature was then reduced to 20 °C and the *E. coli* grown for 16 hours.

**Cell fixing.** For fixed cell samples, mammalian cells and *E. coli* were fixed at the desired time points with 4% paraformaldehyde (PFA) in PBS (Corning) for 20 minutes at room temperature. The fixed cells were washed three times with PBS followed by three times with Milli-Q purified water. *E. coli* samples were spotted onto glass slides and all fixed samples were allowed to air-dry unless otherwise noted.

**Live cell chamber construction**. Live samples cultured on $CaF_2$ coverslips were washed once with PBS and mounted in PBS or Fluorobrite DMEM (Gibco) on a glass microscopy slide (VWR). A double-sided tape spacer (Nitto, San Diego, CA) with a 5 μm thickness was used to keep the cells hydrated and minimize compression of the cell.

**Azidohomoalanine (AHA) incorporation in mammalian cells**. U2OS cells were trypsinized and plated onto $CaF_2$ coverslips. After 6 hours, media was exchanged for methionine, glutamine, and cystine free high-glucose DMEM (Gibco) supplemented with glutamine (4 mM), cystine (0.2 mM) and AHA (5 mM). After 24 hours, the cells were fixed and imaged.

**4-azidomethyl-L-phenylalanine (AzmF) incorporation.** AzmF incorporation as adapted from Bazewicz et al.[25] B.95ΔAΔfabR *E. coli*[26] (Yale *E. coli* Genetic Stock Center, New Haven, CT) were made chemically competent[27] and co-transformed with pET28a-sfGFP TAG150 and pDule-pCNF, gifts from Ryan Mehl (Addgene plasmid #85493 and #85494).[28] A single colony was selected and used to inoculate 5 mL of LB. The starter was grown overnight at 37 °C and 300 rpm shaking. 1 mL of the starter was used to inoculate 20 mL of LB with kanamycin (50 μg/mL) and grown at 37 °C until OD600 ~0.5-0.6 when AzmF (Chem Impex, Wood Dale, IL) was added to 2 mM and IPTG to 1 mM. The sample was kept at 37 °C with shaking at 300 rpm for 20-24 hours then collected via centrifugation at 3900 rpm. The pellet was placed on a glass slide, allowed to dry for 20 minutes, and imaged on the OPTIR directly.

**OPTIR data collection**. All imaging was performed as previously described[18] on a mIRage-LS IR microscope (Photothermal Spectroscopy Corporation, Santa Barbara, CA) integrated with a four-module-pulsed quantum cascade laser (QCL) system (Daylight Solutions, San Diego, CA) with a tunable range from 932 $cm^{-1}$ to 2348 $cm^{-1}$ unless otherwise specified. Briefly, brightfield optical images were collected using a low magnification 10X refractive objective with a working distance of 15 mm. Spectra and infrared images were collected in co-propagating mode unless otherwise specified using a 40X Cassegrain objective with a working distance of 8 mm. Fixed cell spectra and images were collected in standard (epi) mode and live cell spectra and images were collected in transmission mode. Data was collected with an IR laser power of 20% and a probe power in the range of 5-11%. For live cells under our collection conditions, we have AC values between 5 and 50 mV with a DC voltage of ~3.5 V and a detector gain of 5x corresponding to temperature changes between 0.3 and 3 K. All spectra and images were collected using PTIR Studio 4.5 (Photothermal Spectroscopy Corporation). Image acquisition time for multispectral images was 2-5 minutes per frequency for a total acquisition time of 10-25 minutes per cell. For hyperspectral images, a step size of 500 nm, the maximum resolution of the instrument**,** and one acquisition was used.

**Organism imaging.** *H. exemplaris* tardigrades (Carolina Biological Supply, Burling, NC) were cultured in spring water (Poland Spring, Poland, ME) according to published tardigrade culturing protocol.[29] Single tardigrades were collected using a 200 uL pipette tip and deposited onto a glass microscopy slide (VWR) in 30 uL of spring water with double-sided tape spacers (Nitto) with a 5 µm thickness. Tardigrades were covered with a 350 µm thick $CaF_2$ coverslip and imaged immediately.

Zebrafish embryos were selected 48 hours after fertilization and anesthetized using 0.4% tricaine solution (Ward's Science, Rochester, NY). Embryos were placed directly on a microscope slide in 20 µL of E3 medium with tricaine[30] and imaged in epi mode.

**Data analysis.** Images were processed in Fiji (NIH, Bethesda, MD).[31] Spectra were analyzed in IGOR Pro 9 (Wavemetrics, Portland, OR). Live and fixed cell ratio images for both multispectral[18] and hyperspectral[17] images were generated in Python 3.10 in Colab (Google, Mountain View, CA)[32] as previously described.[17,18] To account for overlapping signals of other biomolecules, the ratio images were corrected using the correction protocol adapted from Shi et al,[3] This protocol removes contribution from the amide I by dividing the intensity of the wavenumber at which lipid signal is collected (${}^{13}C=O$ or ${}^{12}C=O$) by the intensity at the amide I (1655 $cm^{-1}$). These values are collected per cell across all time points and averaged to create a correction value with which to subtract off overlapping amide-I for lipid intensities.

Fixed cell ${}^{13}C=O/{}^{12}C=O$ multispectral ratio images were corrected for the amide-I intensity using Equation 1:

$$\frac{{}^{13}C}{{}^{12}C}\ \text{ester carbonyl intensity} = \frac{A_{{}^{13}C=O} - bA_{\text{Amide I}}}{A_{{}^{12}C=O}} \qquad (1)$$

Where $A$ is the signal intensity of the frequency of the indicated biomolecule. The ${}^{12}C=O$ stretch is at 1747 $cm^{-1}$ for adipocytes. The ${}^{13}C=O$ stretch is at 1703 $cm^{-1}$. The variable $b$ is the correction value for the amide-I intensity, with $b$ being 0.31 for adipocytes. Fixed cell ratios were only performed on regions with sufficient ${}^{12}C=O$ signal intensity, defined as regions with 5% of the maximum value of ${}^{12}C=O$ signal for adipocytes.

Hyperspectral ratio images were corrected with Equation 2:

$$\frac{{}^{13}C}{{}^{12}C}\ \text{ester carbonyl intensity} = \frac{\bar{A}_{1693-1713} - b\,\bar{A}_{1645-1655}}{\bar{A}_{1737-1757}} \qquad (2)$$

Where $\bar{A}$ is the average signal intensity over the indicated frequencies. $\bar{A}$ was calculated from full spectra of fixed, control adipocytes. The variable $b$ is the correction value for the amide-I intensity, with $b$ being 0.31 for adipocytes. Fixed cell ratios (eq. 2) were only performed on regions of the cell that had lipid, defined as a ${}^{12}C$ lipid ester carbonyl intensity of 0.025 or greater after vector normalization.

## RESULTS AND DISCUSSION

**Data collection methods and suitability.** Our OPTIR instrument, a commercially available mIRage-LS from Photothermal Spectroscopy Corporation, can collect data in two primary formats: full spectra and single frequency imaging. The spectral coverage of the instrument can be customized by the selected IR laser; our instrument covers a range of 932 $cm^{-1}$ to 2348 $cm^{-1}$ with a gap between 1816 $cm^{-1}$ and 1992 $cm^{-1}$. Full spectra (Fig. 1A) can be collected in an ad-hoc fashion or using an array. Using an array enables the construction of hyperspectral images wherein each pixel of the image contains a full IR spectrum (Fig. 1B). Alternatively, an array can be used to collect images at a single frequency or a few frequencies of interest (multispectral images) (Fig. 1C). Multispectral images are generated by either collecting single frequency images in sequence and stacking them together or by an interleaving method where a row of pixels is collected at one frequency and then again at each additional frequency before imaging the next row of pixels.

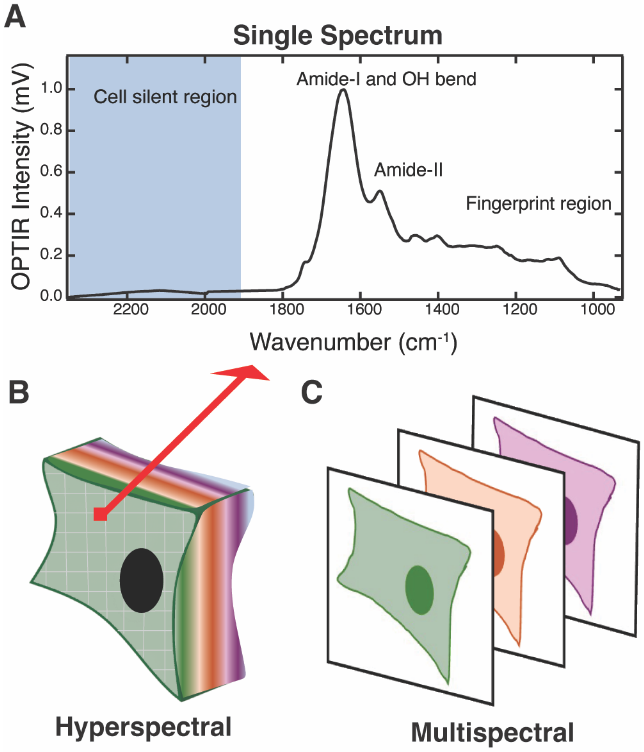

**Figure 1.** Hyperspectral vs. Multispectral Imaging. (A) Representative spectrum of a hydrated biological sample. The cell silent region is shown in blue. (B) Hyperspectral OPTIR map of a cell, where a full IR spectrum is collected in each 500 x 500 nm pixel. (C) Multispectral imaging where an image is collected at several discrete IR frequencies of interest.

OPTIR is compatible with a variety of organisms, cells, and tissue types.[12] Notable IR bands in a generic biological sample (Fig. 1A) include the water bend (1640 $cm^{-1}$, broad), the water bend-libation combination band (2150 $cm^{-1}$, broad, weak), the amide-I (1615-1690 $cm^{-1}$) and amide-II (~1550 $cm^{-1}$) of proteins, the CH deformation of proteins and lipids (1300-1500 $cm^{-1}$), nucleic acid and lipid phosphate stretches (~1080 $cm^{-1}$), and others.[5,33,34] Using these bands, different cell types can be distinguished.[35–37] We compared average fixed cell spectra collected in epi copropagating mode of full hyperspectral maps of three commonly used model cell lines:

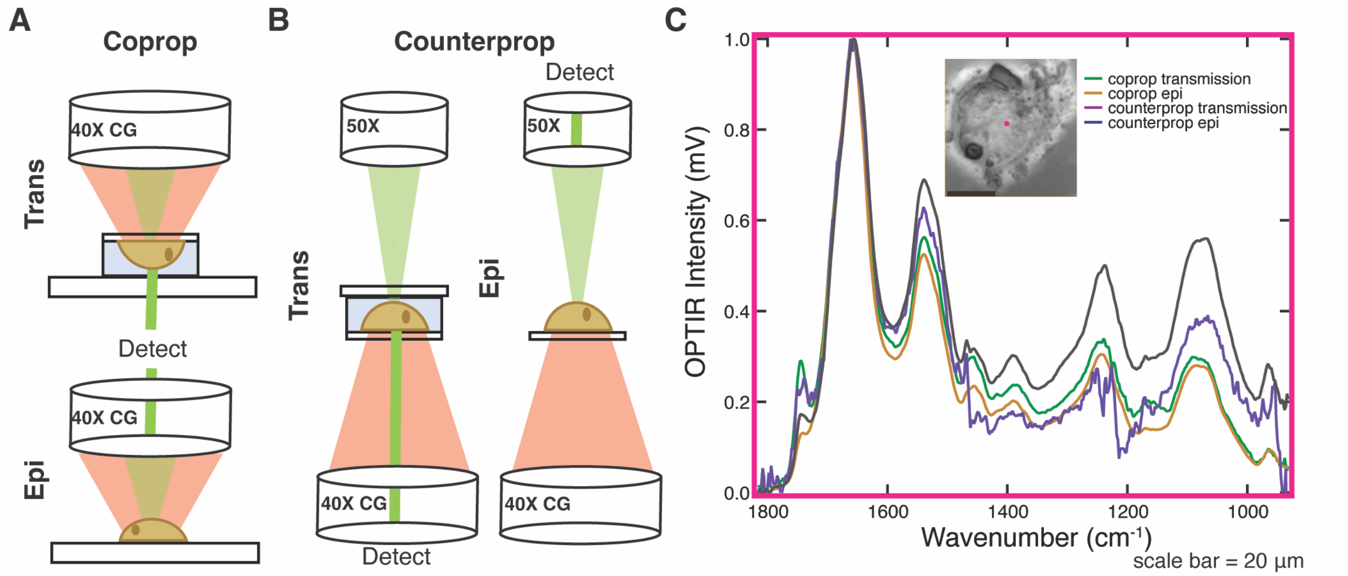

**Figure 2.** Signal-to-noise (S/N) ratio of different modes of data collection. The visible laser of the OPTIR can be collected in both and epi and trans geometry for both (A) copropagation and (B) counterpropagation geometry of the infrared laser. (C) Example spectra from a fixed Huh-7 cell collected at the same spot (x, y, and z held constant, pink) in coprop transmission (green) and epi (yellow) and counterprop transmission (purple) and epi (blue).

osteosarcoma line U2OS, hepatoma line Huh-7, and adipocyte model line differentiated 3T3-L1, and made full assignments (Fig. S1). The average spectra were similar with near identical amide-I and amide-II bandwidths and ratios. Although previous work[35] has shown differences in amide-I to amide-II ratios and bandwidths between cell lines, that work distinguished cancerous and benign cells from tissue while our samples were all cultured cancer derived cell lines. Within the cancer derived lines (Fig. S1) the ratio of lipid bands as compared to the protein bands was dramatically different. Differentiated 3T3-L1 cells, which are an adipocyte-like cell lines and therefore lipid rich, had the highest lipid to protein ratio. U2OS cells had the lowest. There were also notable differences in the CH deformation region, pointing at differences in protein, lipid, and carbohydrate composition.

To determine the optimal mode for imaging biological samples, the signal-to-noise (S/N) ratio of the different OPTIR imaging modalities was evaluated. The OPTIR instrument's laser paths can be set up in two modes. In copropagating mode (coprop, Fig. 2A), the infrared and visible lasers are collinear. The visible laser can be collected for analysis either in epi or transmission mode. In counterpropagating mode (counterprop, Fig. 2B), the visible and infrared lasers are split with the visible laser entering from the top objective and the infrared from the bottom objective. This can again be collected in epi or transmission mode. The noise of each modality was determined by collecting three reference spectra of a calcium fluoride coverslip, which has no mid-IR absorbance, for each modality (Fig. S2). Each spectrum is the average of three acquisitions with an IR power of 20%, probe power of 11%, and detector gain of 1x. We report average root mean square noise across covered frequencies: 0.02 mV for coprop transmission, 0.01 mV for coprop epi, 0.31 mV for counterprop transmission and 0.04 mV for counterprop epi. Smaller signals can be detected by additional signal averaging. Using the fixed cell as a representative signal this gives S/N ratios at 1658 cm$^{-1}$ of ~514 for coprop trans, ~2760 for coprop epi, ~33 for counterprop trans, and ~1150 for counterprop epi. In all modalities, the S/N ratio of coprop is greater than counterprop, and this difference can be visualized in spectra of fixed cells across the spectral range (Fig. 2C). Because of the higher S/N ratio, we commonly collect data in coprop mode. However, counterprop is not without advantages as it has a slightly improved spatial resolution. This is due to the improved numerical aperture of the 50x refractive objective used for the visible light in counterprop (Fig. 2B) as compared to the 40X Cassegrain objective used for the infrared/visible light (Fig. 2A). It also resolves minor issues caused by changing between objectives when comparing brightfield or fluorescence images to OPTIR images.

Epi is generally used for fixed cell work while transmission is necessary for live cell work where the lasers must pass through coverglass and aqueous solution before interacting with a living cell. Live cells are grown on coverslips and mounted onto standard glass slides using a double-sided adhesive spacer with a pathlength of 5-10 µm to limit water background (Fig. 2A-B). The chamber is filled with either PBS or media to ensure cell viability without IR interfering additives such as phenol red or protein and lipid found in fetal bovine serum. In counterprop mode, the cells can be grown on either glass or calcium fluoride coverslips, while the coprop mode is only compatible with calcium fluoride coverslips. However, counterprop mode necessitates a slightly more complex sample assembly than coprop mode. Because the lasers must be focused through objectives from both sides, a calcium fluoride coverslip must be mounted on to a glass cover slip rather than a glass slide, decreasing ease of handling and chamber construction (Fig. 2B). In our experience, imaging biological samples in counterprop with transmission collection has significantly lower signal to noise compared to the same spot collected in coprop transmission mode (Fig. 2C), which is consistent with our S/N analysis (Fig. S2). Therefore, our preferred live cell imaging modality is coprop transmission (Fig. 2A).

**Multispectral vs. hyperspectral imaging.** Although hyperspectral images are data rich, due to the long collection times, on the order of hours, they are only compatible with

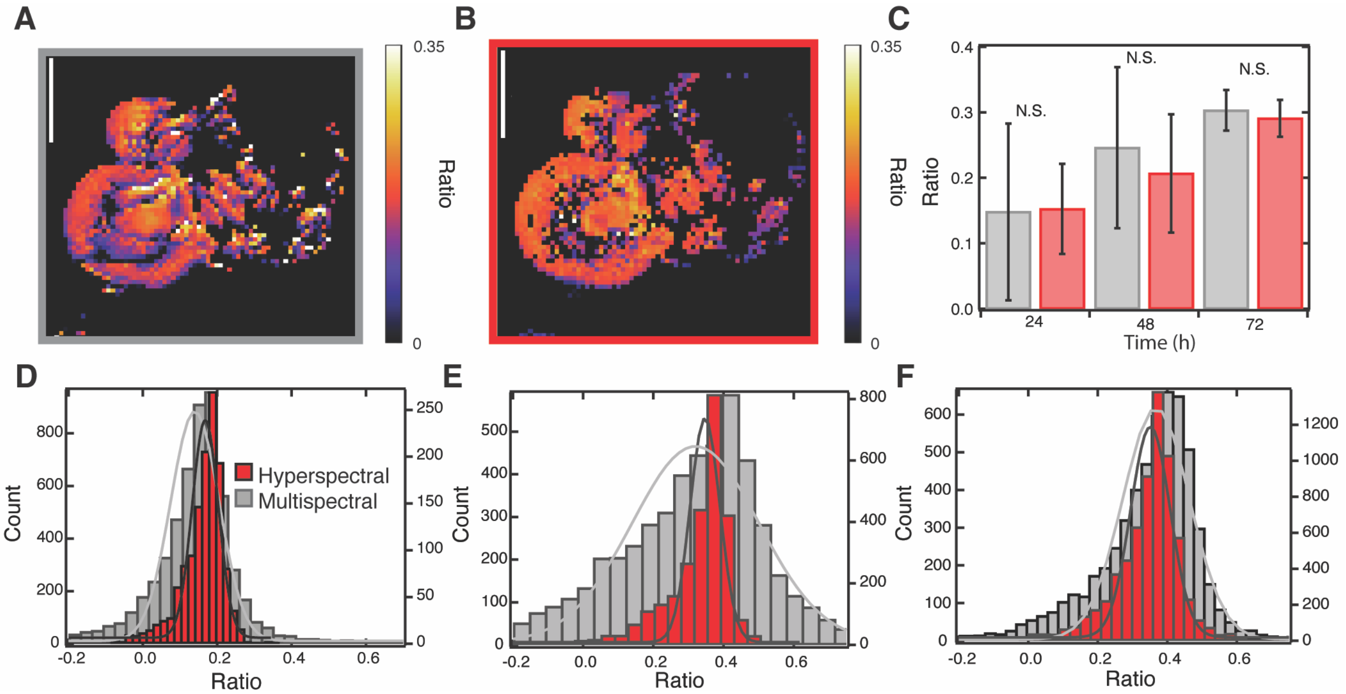

**Figure 3.** Hyperspectral and multispectral ratio imaging comparison. Representative (A) multispectral and (B) hyperspectral ratio image at 24 hours post $^{13}$C glucose feeding. Scale bars equal to 10 µm. A pixel size of 250 nm with a scan speed of 150 µm/s was used for the multispectral imaging and a step size of 500 nm was used for hyperspectral imaging. (C) Averages of the ratio of $^{13}$C lipid to $^{12}$C lipid for hyperspectral (red) and multispectral (grey) images (n=3 cells per timepoint). Histograms of the ratio of $^{13}$C lipid to $^{12}$C lipid as calculated from hyperspectral (red) and multispectral (grey) images in three differentiated 3T3-L1 cells at (D) 24, (E) 48, and (F) 72 hours after feeding with $^{13}$C glucose. See methods for ratio calculation.

fixed cells. Thus, live cell imaging necessitates multispectral imaging or the collection of few ad hoc full spectra. Hyperspectral data collected in fixed cells can be used to identify specific frequencies of interest for multispectral imaging and, for dynamic processes, to determine anticipated changes in IR absorbance between different conditions. Nevertheless, significant data is lost when information is only collected at 2-5 frequencies. Do multispectral images match hyperspectral images? How accurate is multispectral data processing at correcting for background and replicating trends seen with hyperspectral data?

To answer these questions, we compared hyperspectral and multispectral images of fixed differentiated 3T3-L1 cells fed $^{13}$C glucose. In differentiated 3T3-L1 cells, the $^{13}$C glucose is metabolized through glycolysis and then *de novo* lipogenesis over the span several days. The $^{13}$C glucose is primarily incorporated into triglycerides, which are stored inside of lipid droplets.[17,18] The metabolic rate and spatial distribution can be tracked as a ratio of the $^{13}$C:$^{12}$C ester carbonyl of triglycerides. Hyperspectral images were thresholded to only include pixels with significant native lipid signal; this was defined as an average intensity over the range of 1737-1757 cm$^{-1}$ of at least 2.5% of the vector normalized spectrum. A ratio image was calculated at the remaining pixels as the average intensity of the labeled $^{13}$C=O lipid band (1693-1713 cm$^{-1}$) over native $^{12}$C=O lipid band (1737-1757 cm$^{-1}$) after correction for overlap with the amide-I band (Equation 1). A similar protocol was followed for the multispectral images except that single frequency images were collected at only the native and labeled lipid bands and the protein band, 1747, 1703, and 1655 cm$^{-1}$, respectively (Equation 2) and a threshold of 5 % of maximum lipid intensity was used. Multispectral images at the three frequencies could be collected in 5-15 minutes total for a pixel size of 250 nm while hyperspectral required 15-24 hours for a pixel size of 500 nm. We found qualitatively good agreement between the hyperspectral and multispectral ratio images (Fig. 3A-B).

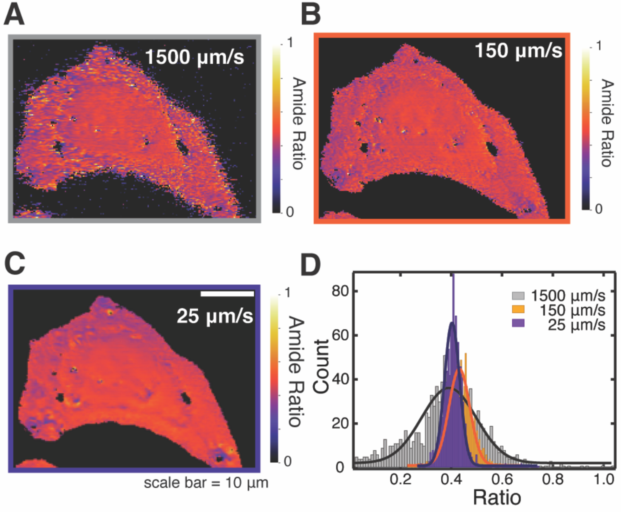

**Figure 4.** Scan speed determines noise. Fixed Huh-7 cell multispectral ratio images of amide-II to amide-I at scan speeds of (A) 1500 µm/s, (B) 150 µm/s and (C) 25 µm/s. Pixel size was 250 nm. (D) Histograms of the ratios of pixels shown in A-C.

The average of three hyperspectral images of cells as compared to the three matching multispectral images showed good agreement (Fig. 3C) ($p>0.15$ at each timepoint in a paired t-test). However, a histogram of the ratios obtained at

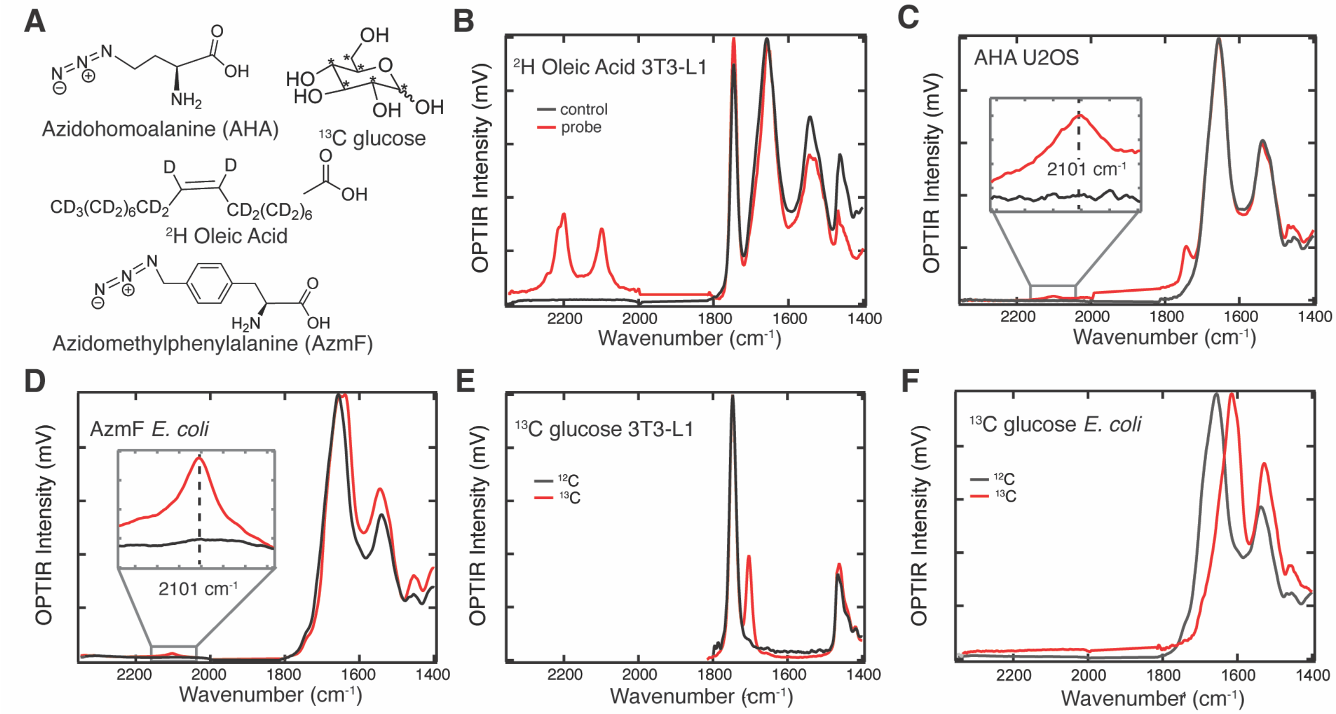

**Figure 5.** Metabolic probes in biological systems. (A) Chemical structures of infrared probes. (B) Representative spectra in a fixed differentiated 3T3-L1 cell with (red) and without (black) feeding deuterated oleic acid (24 hrs, 60 μm). (C) Representative spectra of a fixed U2OS cell with (red) and without (black) feeding azidohomoalanine (24 hrs, 5 mM). Inset: Azide mode of AHA. (D) Average spectra of dried *E. coli* expressing sfGFP with AzmF incorporated at position 150 (red) and control *E. coli* (black). Inset: Azide mode of AzmF. (E) Representative spectra of a fixed differentiated 3T3-L1 cell with (red) and without (black) feeding of $^{13}$C glucose (72 hrs, 4.5 g/L). The control spectrum was collected on a previous mIRage OPTIR model.[17] No data in cell silent region. (F) Average spectra of fixed *E. coli* after feeding $^{12}$C glucose media (black) or $^{13}$C glucose media (red).

each pixel reveals systematic differences between the hyperspectral and multispectral images. Ratios generated from the multispectral images had a wider distribution than those calculated from the hyperspectral images (Fig. 3D-F). A possible explanation for the wider distribution of ratios in the multispectral data is that small peak shifts in the native lipid band (caused by differences in lipid composition across the cell) are detected in a single frequency multispectral image but not detected in the hyperspectral images which use the average frequency of a 20 cm$^{-1}$ bandwidth. However, narrowing the average range for the for the hyperspectral image processing to 2 cm$^{-1}$, similar to the ~1.1 cm$^{-1}$ laser bandwidth used for multispectral images, does not significantly increase the FWHM of the Gaussian (Fig. S3). Similarly, adjusting the spatial resolution via binning the multispectral image pixels to 500 nm to match the hyperspectral images does not influence width (Fig. S4).

Instead, differences between hyperspectral and multispectral imaging are caused by the increased scan speeds used in multispectral imaging and possibly error in the stage movement. Hyperspectral images collected at 500 nm resolution have a “scan speed” of less than 0.06 μm/s given that each spectrum takes approximately 8 s to collect. We suspect that this greatly reduces stage vibrations and other sources of error. To prove this, we conducted multispectral imaging of amide-II to amide-I ratio at a low scan rate on fixed Huh-7 cells and saw narrowing of the histograms (Fig. 4). However, imaging time was increased by a factor of 10. Together, this showcases that multispectral imaging is an excellent tool with speed several orders of magnitude faster than hyperspectral imaging, albeit with slightly increased error. Multispectral imaging can therefore be reliably used for live cell imaging.

**Live cell imaging.** Spectra collected in live cells share many features with those collected in fixed cells with the addition of a dominant water band (Fig. S5). The water band can be corrected for in multispectral ratio images via a straightforward linear correction, although complete preservation of all structural information contained in the amide-I band is not possible.[18] We have previously found good agreement between $^{13}$C/$^{12}$C lipid ratios in fixed and live Huh-7 and 3T3-L1 cells.[17,18] In cases where bands of significant interest are obstructed by the water bend (i.e. protein secondary structure studies), $D_2O$ can be used in place of $H_2O$ as the D-O-D and D-O-H bends are significantly shifted.[38,39] Alternatively, the amide-I band can be shifted by IR labeling (Fig. 5).

**Infrared probes in OPTIR.** While the intrinsic IR modes of biological molecules can be used to assign a variety of cellular components (Fig. S1), they lack the specificity to track specific molecules in the cellular milieu. Vibrational probes can be used to track a specific cellular process[3,4] or biological molecule[40] of interest and in some cases can even reveal local structural and/or environmental information (Fig. 5A). IR probes are most useful when there is not significant cellular background in the spectral region of the vibrational mode. This makes the cell silent window particularly attractive (Fig. 1A). We[18] and others[41] have used deuterated fatty acids to track metabolic pathways such as fatty acid scavenging and esterification. C-D stretches appear in the cell silent region and are sensitive to fatty acid unsaturation (Fig. 5B). Others have followed lipid[15] and carbohydrate[19] metabolism via azide labeled precursors. The azide moiety has a strong infrared absorbance at 2100 cm$^{-1}$ in the cellular silent region where there is no significant interference from other cellular biomolecules.

Here we demonstrate global and site-specific protein labeling using azide probes azidohomoalanine (AHA) and 4-azidomethyl-L-phenylalanine (AzmF), respectively. AHA is a methionine analog that is readily incorporated into proteins via traditional protein synthesis.[42] By employing a methionine auxotroph in a methionine-free environment, all methionine residues in newly synthesized proteins should be replaced with AHA residues. After feeding, AHA signal in the cellular silent region was detectable in both *E. coli* and human U2OS cells (Fig. S6, Fig. 5C). In the future, AHA can be used as a general probe of protein synthesis and degradation.

Alternatively, the azide probe AzmF can be incorporated site-specifically into a protein of interest via amber codon suppression.[43] This handle can be used to map the location of the labeled protein, and as the IR signal of AzmF is sensitive to local environment, this probe may serve as a tool for protein localization and structural determination.[25] We incorporated AzmF into overexpressed sfGFP at position 150 in *E. coli* using amber codon suppression.[44] Despite only being incorporated into a single location of a single, overexpressed protein, the AzmF signal was easily detectable in the cell silent region (Fig. 5D).

Vibrational probes can also be well visualized in other regions. For example, we have previously used isotopic precursor $^{13}$C glucose to track lipogenesis via incorporation of the isotope label into cellular lipids (Fig. 5E).[18,45] Feeding $^{13}$C glucose leads to shifts across the cell's infrared profile where $^{13}$C is incorporated. The heavier isotope causes a redshift in vibrations when present as frequency is inversely proportional to reduced mass according to Equation 3:[46]

$$\nu = \frac{1}{2\pi}\sqrt{\frac{k}{\mu}} \qquad (3)$$

where ν is frequency, k is the force constant of the bond, and μ is reduced mass. Shifts in the spectrum, i.e. what biomolecules $^{13}$C is incorporated into from $^{13}$C glucose, depend on the metabolism of the cell line in question. When $^{13}$C glucose is fed to *E. coli* cells, the bulk of the carbon is used for protein synthesis. *E coli* grown in $^{13}$C glucose minimal media have a shifted amide-I and II band highlighting this (Fig. 5F). Conversely, in mammalian fat (differentiated 3T3-L1) and liver (Huh-7) cells the bulk of the glucose is directed to *de novo* lipogenesis, leading to the appearance of peaks associated with $^{13}$C labeled lipids (Fig. 5E).[18] The most notable of these is the red-shifted lipid ester carbonyl stretch at 1703 cm$^{-1}$. Interestingly, the unlabeled lipid ester carbonyl stretch appears at slightly different positions in Huh-7 (1744 cm$^{-1}$) and differentiated 3T3-L1 (1747 cm$^{-1}$) cells hinting at different lipid compositions (Fig. S1). Upon labeling, the lipid ester carbonyl peak shifts to 1703 cm$^{-1}$ for both cell types suggesting that *de novo* lipogenesis over the time frame studied (72 hours) leads to more homogenous lipids, likely triacylglycerol (Fig. 5E).[47]

**Organism imaging.** OPTIR is also compatible with whole organism imaging.[12] We predict that dynamic measurements taken via multispectral imaging and the flexibility and non-perturbative nature of IR probes will allow for better understanding of in organism metabolism and catabolism. Here we demonstrate that OPTIR can be collected in two model organisms, zebrafish embryo and *H. exemplaris* tardigrades (Fig. 6). Future studies could examine protein synthesis during tardigrade desiccation or changing IR signals in the embryo as its cells differentiate. IR probes could be used to follow metabolism in these organisms or localize specific proteins without the disruption caused by fluorescent tags.[3]

## CONCLUSION

This work demonstrates the flexibility of OPTIR as a tool for understanding biological systems. We have been able to showcase a variety of collection methods and confirm that multifrequency imaging collected in sequence at carefully selected frequencies can provide information equivalent to hyperspectral imaging at 20-30x the speed (minutes compared to 10-20 hours). This allows for detailed live cell imaging. Moreover, the development and application of IR active probes allow for investigation of specific proteins and metabolic pathways. Together, these advancements make OPTIR a powerful technique for cellular systems and introduces the possibility for future work to bring these probes and this dynamic imaging into whole organisms.

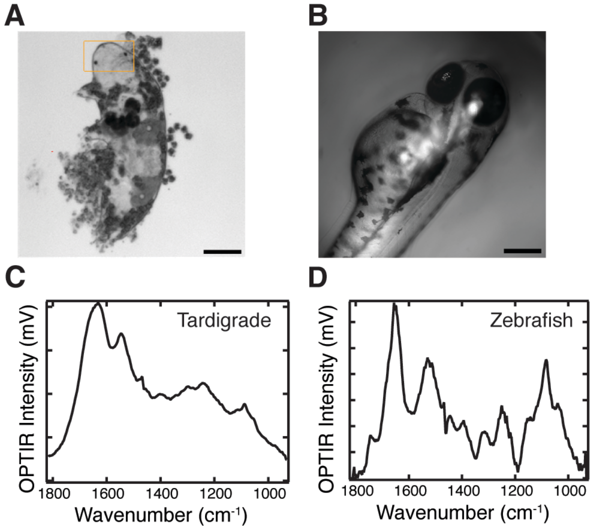

**Figure 6.** Live organism OPTIR. (A) Live tardigrade and (B) zebrafish embryo 48 hours post fertilization and (C-D) corresponding single spectra. Tardigrade collected in coprop transmission and zebrafish in coprop epi. Scale bars are 50 μm.

## ASSOCIATED CONTENT

### Supporting Information

The Supporting Information is available free of charge on the ACS Publications website.

Supplemental methods of AHA incorporation, supplemental Figure S1-S6. (PDF)

## AUTHOR INFORMATION

### Corresponding Author

* Caitlin M. Davis c.davis@yale.edu

### Notes

The authors declare no competing financial interest.

## ACKNOWLEDGMENTS

This work was supported by the Arnold and Mabel Beckman Foundation. Hepatocyte research was conducted while Caitlin Davis was a Hevolution/AFAR New Investigator Awardee in Aging Biology and Geroscience Research. Adipocyte and zebrafish research was supported by National Institutes of Health (NIH) grant R35 GM151146. Tardigrade research was supported by NSF CAREER award MCB-2338323. S. O. S. and A. E. C. were partially supported by the NIH under training grant T32

GM008283. S. O. S. was partially supported by a National Science Foundation Graduate Research Fellowship under grant DGE-2139841. The authors thank Brahmmi Patel and Cailin Hoang for providing the zebrafish embryos and Marisa Barilla for tardigrade culturing.

## REFERENCES

(1) Diem, M.; Romeo, M.; Boydston-White, S.; Miljkovic, M.; Matthaus, C. A Decade of Vibrational Micro-Spectroscopy of Human Cells and Tissue (1994-2004). *Analyst* **2004**, *129* (10), 880–885. https://doi.org/10.1039/b408952a.

(2) Jones, R. R.; Hooper, D. C.; Zhang, L.; Wolverson, D.; Valev, V. K. Raman Techniques: Fundamentals and Frontiers. *Nanoscale Res. Lett.* **2019**, *14* (1), 231. https://doi.org/10.1186/s11671-019-3039-2.

(3) Shi, L.; Liu, X.; Shi, L.; Stinson, H. T.; Rowlette, J.; Kahl, L. J.; Evans, C. R.; Zheng, C.; Dietrich, L. E. P.; Min, W. Mid-Infrared Metabolic Imaging with Vibrational Probes. *Nat. Methods* **2020**, *17* (8), 844–851. https://doi.org/10.1038/s41592-020-0883-z.

(4) Wei, L.; Hu, F.; Chen, Z.; Shen, Y.; Zhang, L.; Min, W. Live-Cell Bioorthogonal Chemical Imaging: Stimulated Raman Scattering Microscopy of Vibrational Probes. *Acc. Chem. Res.* **2016**, *49* (8), 1494–1502. https://doi.org/10.1021/acs.accounts.6b00210.

(5) Barth, A. Infrared Spectroscopy of Proteins. *Biochim. Biophys. Acta BBA - Bioenerg.* **2007**, *1767* (9), 1073–1101. https://doi.org/10.1016/j.bbabio.2007.06.004.

(6) Davis, C. M.; Reddish, M. J.; Dyer, R. B. Dual Time-Resolved Temperature-Jump Fluorescence and Infrared Spectroscopy for the Study of Fast Protein Dynamics. *Spectrochim. Acta. A. Mol. Biomol. Spectrosc.* **2017**, *178*, 185–191. https://doi.org/10.1016/j.saa.2017.01.069.

(7) Zhu, Y.; Ge, X.; Ni, H.; Yin, J.; Lin, H.; Wang, L.; Tan, Y.; Prabhu Dessai, C. V.; Li, Y.; Teng, X.; Cheng, J.-X. Stimulated Raman Photothermal Microscopy toward Ultrasensitive Chemical Imaging. *Sci. Adv.* **2023**, *9* (43), eadi2181. https://doi.org/10.1126/sciadv.adi2181.

(8) Schnell, M.; Mittal, S.; Falahkheirkhah, K.; Mittal, A.; Yeh, K.; Kenkel, S.; Kajdacsy-Balla, A.; Carney, P. S.; Bhargava, R. All-Digital Histopathology by Infrared-Optical Hybrid Microscopy. *Proc. Natl. Acad. Sci. U. S. A.* **2020**, *117* (7), 3388–3396. https://doi.org/10.1073/pnas.1912400117.

(9) Centrone, A. Infrared Imaging and Spectroscopy Beyond the Diffraction Limit. *Annu. Rev. Anal. Chem.* **2015**, *8* (1), 101–126. https://doi.org/10.1146/annurev-anchem-071114-040435.

(10) Zhang, D.; Li, C.; Zhang, C.; Slipchenko, M. N.; Eakins, G.; Cheng, J.-X. Depth-Resolved Mid-Infrared Photothermal Imaging of Living Cells and Organisms with Submicrometer Spatial Resolution. *Sci. Adv.* **2016**, *2* (9), e1600521. https://doi.org/10.1126/sciadv.1600521.

(11) Xia, Q.; Yin, J.; Guo, Z.; Cheng, J.-X. Mid-Infrared Photothermal Microscopy: Principle, Instrumentation, and Applications. *J. Phys. Chem. B* **2022**, *126* (43), 8597–8613. https://doi.org/10.1021/acs.jpcb.2c05827.

(12) Gvazava, N.; Konings, S. C.; Cepeda-Prado, E.; Skoryk, V.; Umeano, C. H.; Dong, J.; Silva, I. A. N.; Ottosson, D. R.; Leigh, N. D.; Wagner, D. E.; Klementieva, O. Label-Free High-Resolution Photothermal Optical Infrared Spectroscopy for Spatiotemporal Chemical Analysis in Fresh, Hydrated Living Tissues and Embryos. *J. Am. Chem. Soc.* **2023**, *145* (45), 24796–24808. https://doi.org/10.1021/jacs.3c08854.

(13) Spadea, A.; Denbigh, J.; Lawrence, M. J.; Kansiz, M.; Gardner, P. Analysis of Fixed and Live Single Cells Using Optical Photothermal Infrared with Concomitant Raman Spectroscopy. *Anal. Chem.* **2021**, *93* (8), 3938–3950. https://doi.org/10.1021/acs.analchem.0c04846.

(14) Romeo, M. J.; Boydston-White, S.; Matthäus, C.; Miljković, M.; Bird, B.; Chernenko, T.; Diem, M. Vibrational Microspectroscopy of Cells and Tissues. In *Biomedical Vibrational Spectroscopy*; John Wiley & Sons, Ltd, 2008; pp 121–152. https://doi.org/10.1002/9780470283172.ch6.

(15) Bai, Y.; Camargo, C. M.; Glasauer, S. M. K.; Gifford, R.; Tian, X.; Longhini, A. P.; Kosik, K. S. Single-Cell Mapping of Lipid Metabolites Using an Infrared Probe in Human-Derived Model Systems. *Nat. Commun.* **2024**, *15* (1), 350. https://doi.org/10.1038/s41467-023-44675-0.

(16) Onsager, L. Reciprocal Relations in Irreversible Processes. I. *Phys. Rev.* **1931**, *37* (4), 405–426. https://doi.org/10.1103/PhysRev.37.405.

(17) Shuster, S. O.; Burke, M. J.; Davis, C. M. Spatiotemporal Heterogeneity of De Novo Lipogenesis in Fixed and Living Single Cells. *J. Phys. Chem. B* **2023**, *127* (13), 2918–2926. https://doi.org/10.1021/acs.jpcb.2c08812.

(18) Castillo, H. B.; Shuster, S. O.; Tarekegn, L.; Davis, C. Oleic Acid Differentially Affects Lipid Droplet Storage of de Novo Synthesized Lipids in Hepatocytes and Adipocytes. *Chem. Commun.* **2024**. https://doi.org/10.1039/D3CC04829B.

(19) Xia, Q.; Perera, H. A.; Bolarinho, R.; Piskulich, Z. A.; Guo, Z.; Yin, J.; He, H.; Li, M.; Ge, X.; Cui, Q.; Ramström, O.; Yan, M.; Cheng, J.-X. Click-Free Imaging of Carbohydrate Trafficking in Live Cells Using an Azido Photothermal Probe. bioRxiv **2024**. https://doi.org/10.1101/2024.03.08.584185.

(20) Klementieva, O.; Sandt, C.; Martinsson, I.; Kansiz, M.; Gouras, G. K.; Borondics, F. Super-Resolution Infrared Imaging of Polymorphic Amyloid Aggregates Directly in Neurons. *Adv. Sci.* **2020**, *7* (6), 1903004. https://doi.org/10.1002/advs.201903004.

(21) Flynn, J. D.; Gimmen, M. Y.; Dean, D. N.; Lacy, S. M.; Lee, J. C. Terminal Alkynes as Raman Probes of α-Synuclein in Solution and in Cells. *Chembiochem Eur. J. Chem. Biol.* **2020**. https://doi.org/10.1002/cbic.202000026.

(22) Wei, L.; Hu, F.; Shen, Y.; Chen, Z.; Yu, Y.; Lin, C.-C.; Wang, M. C.; Min, W. Live-Cell Imaging of Alkyne-Tagged Small Biomolecules by Stimulated Raman Scattering. *Nat. Methods* **2014**, *11* (4), 410–412. https://doi.org/10.1038/nmeth.2878.

(23) Alsabeeh, N.; Chausse, B.; Kakimoto, P. A.; Kowaltowski, A. J.; Shirihai, O. Cell Culture Models of Fatty Acid Overload: Problems and Solutions. *Biochim. Biophys. Acta* **2018**, *1863* (2), 143–151. https://doi.org/10.1016/j.bbalip.2017.11.006.

(24) Kleinfeld, A. M.; Prothro, D.; Brown, D. L.; Davis, R. C.; Richieri, G. V.; DeMaria, A. Increases in Serum Unbound Free Fatty Acid Levels Following Coronary Angioplasty. *Am. J. Cardiol.* **1996**, *78* (12), 1350–1354. https://doi.org/10.1016/S0002-9149(96)00651-0.

(25) Bazewicz, C. G.; Liskov, M. T.; Hines, K. J.; Brewer, S. H. Sensitive, Site-Specific, and Stable Vibrational Probe of Local Protein Environments: 4-Azidomethyl-l-Phenylalanine. *J. Phys. Chem. B* **2013**, *117* (30), 8987–8993. https://doi.org/10.1021/jp4052598.

(26) Mukai, T.; Hoshi, H.; Ohtake, K.; Takahashi, M.; Yamaguchi, A.; Hayashi, A.; Yokoyama, S.; Sakamoto, K. Highly Reproductive Escherichia Coli Cells with No Specific Assignment to the UAG Codon. *Sci. Rep.* **2015**, *5*, 9699. https://doi.org/10.1038/srep09699.

(27) *Preparation of Calcium Competent Escherichia coli and Heat-Shock Transformation | jemi.microbiology.ubc.ca*. https://ujemi.microbiology.ubc.ca/node/127 (accessed 2024-06-19).

(28) Miyake-Stoner, S. J.; Miller, A. M.; Hammill, J. T.; Peeler, J. C.; Hess, K. R.; Mehl, R. A.; Brewer, S. H. Probing Protein Folding Using Site-Specifically Encoded Unnatural Amino Acids as FRET Donors with Tryptophan. *Biochemistry* **2009**, *48* (25), 5953–5962. https://doi.org/10.1021/bi900426d.

(29) Boothby, T. C.; Tapia, H.; Brozena, A. H.; Piszkiewicz, S.; Smith, A. E.; Giovannini, I.; Rebecchi, L.; Pielak, G. J.; Koshland, D.; Goldstein, B. Tardigrades Use Intrinsically Disordered Proteins to Survive Desiccation. *Mol. Cell* **2017**, *65* (6), 975-984.e5. https://doi.org/10.1016/j.molcel.2017.02.018.

(30) Westerfield, M.; Westernfield, M. *The Zebrafish Book: A Guide for the Laboratory Use of Zebrafish (Danio Rerio)*, 5th ed.; University of Oregon: Eugene, 2007.

(31) Schindelin, J.; Arganda-Carreras, I.; Frise, E.; Kaynig, V.; Longair, M.; Pietzsch, T.; Preibisch, S.; Rueden, C.; Saalfeld, S.; Schmid, B.; Tinevez, J.-Y.; White, D. J.; Hartenstein, V.; Eliceiri, K.; Tomancak, P.; Cardona, A. Fiji: An Open-Source Platform for

Biological-Image Analysis. *Nat. Methods* **2012**, *9* (7), 676–682. https://doi.org/10.1038/nmeth.2019.

(32) Van Rossum, G.; Drake, F. L. *Python 3 Reference Manual*; CreateSpace: Scotts Valley, CA, 2009.

(33) Derenne, A.; Claessens, T.; Conus, C.; Goormaghtigh, E. Infrared Spectroscopy of Membrane Lipids. In *Encyclopedia of Biophysics*; Roberts, G. C. K., Ed.; Springer: Berlin, Heidelberg, 2013; pp 1074–1081. https://doi.org/10.1007/978-3-642-16712-6_558.

(34) Naumann, D. Infrared Spectroscopy of Cells, Tissues, and Biofluids. In *Encyclopedia of Biophysics*; Roberts, G. C. K., Ed.; Springer: Berlin, Heidelberg, 2013; pp 1057–1065. https://doi.org/10.1007/978-3-642-16712-6_120.

(35) Taylor, S. E.; Cheung, K. T.; Patel, I. I.; Trevisan, J.; Stringfellow, H. F.; Ashton, K. M.; Wood, N. J.; Keating, P. J.; Martin-Hirsch, P. L.; Martin, F. L. Infrared Spectroscopy with Multivariate Analysis to Interrogate Endometrial Tissue: A Novel and Objective Diagnostic Approach. *Br. J. Cancer* **2011**, *104* (5), 790–797. https://doi.org/10.1038/sj.bjc.6606094.

(36) Bird, B.; Romeo, M. J.; Diem, M.; Bedrossian, K.; Laver, N.; Naber, S. Cytology by Infrared Micro-Spectroscopy: Automatic Distinction of Cell Types in Urinary Cytology. *Vib. Spectrosc.* **2008**, *48* (1), 101–106. https://doi.org/10.1016/j.vibspec.2008.03.006.

(37) Martin, F. L.; Kelly, J. G.; Llabjani, V.; Martin-Hirsch, P. L.; Patel, I. I.; Trevisan, J.; Fullwood, N. J.; Walsh, M. J. Distinguishing Cell Types or Populations Based on the Computational Analysis of Their Infrared Spectra. *Nat. Protoc.* **2010**, *5* (11), 1748–1760. https://doi.org/10.1038/nprot.2010.133.

(38) Bonner, O. D.; Curry, J. D. Infrared Spectra of Liquid H2O and D2O. *Infrared Phys.* **1970**, *10* (2), 91–94. https://doi.org/10.1016/0020-0891(70)90003-5.

(39) Venyaminov SYu, null; Prendergast, F. G. Water (H2O and D2O) Molar Absorptivity in the 1000-4000 Cm-1 Range and Quantitative Infrared Spectroscopy of Aqueous Solutions. *Anal. Biochem.* **1997**, *248* (2), 234–245. https://doi.org/10.1006/abio.1997.2136.

(40) Ma, J.; Pazos, I. M.; Zhang, W.; Culik, R. M.; Gai, F. Site-Specific Infrared Probes of Proteins. *Annu. Rev. Phys. Chem.* **2015**, *66* (1), 357–377. https://doi.org/10.1146/annurev-physchem-040214-121802.

(41) Bai, Y.; Zhang, D.; Li, C.; Liu, C.; Cheng, J.-X. Bond-Selective Imaging of Cells by Mid-Infrared Photothermal Microscopy in High Wavenumber Region. *J. Phys. Chem. B* **2017**, *121* (44), 10249–10255. https://doi.org/10.1021/acs.jpcb.7b09570.

(42) Ma, Y.; Di Salvo, M. L.; Budisa, N. Self-Directed in Cell Production of Methionine Analogue Azidohomoalanine by Synthetic Metabolism and Its Incorporation into Model Proteins. In *Noncanonical Amino Acids: Methods and Protocols*; Lemke, E. A., Ed.; Methods in Molecular Biology; Springer: New York, NY, 2018; pp 127–135. https://doi.org/10.1007/978-1-4939-7574-7_7.

(43) Supekova, L.; Zambaldo, C.; Choi, S.; Lim, R.; Luo, X.; Kazane, S. A.; Young, T. S.; Schultz, P. G. The Genetic Incorporation of P-Azidomethyl-l-Phenylalanine into Proteins in Yeast. *Bioorg. Med. Chem. Lett.* **2018**, *28* (9), 1570–1573. https://doi.org/10.1016/j.bmcl.2018.03.055.

(44) Furter, R. Expansion of the Genetic Code: Site-Directed p-Fluoro-Phenylalanine Incorporation in Escherichia Coli. *Protein Sci. Publ. Protein Soc.* **1998**, *7* (2), 419–426.

(45) Shuster, S. O.; Burke, M. J.; Davis, C. M. Spatiotemporal Heterogeneity of De Novo Lipogenesis in Fixed and Living Single Cells. *J. Phys. Chem. B* **2023**. https://doi.org/10.1021/acs.jpcb.2c08812.

(46) Spectral Analysis. In *Infrared Spectroscopy: Fundamentals and Applications*; John Wiley & Sons, Ltd, 2004; pp 45–70. https://doi.org/10.1002/0470011149.ch3.

(47) Ameer, F.; Scandiuzzi, L.; Hasnain, S.; Kalbacher, H.; Zaidi, N. De Novo Lipogenesis in Health and Disease. *Metabolism* **2014**, *63* (7), 895–902. https://doi.org/10.1016/j.metabol.2014.04.003.

Insert Table of Contents artwork here